Correction for Attenuation in Technetium-99m-HMPAO SPECT Brain Imaging

Brad J. Kemp, Frank S. Prato, Geoff W. Dean, R. Larry Nicholson, and Lionel Reese

Department of Nuclear Medicine, St. Joseph's Health Centre, Lawson Research Institute and The University of Western Ontario, London, Ontario, Canada; and Department of Nuclear Medicine, Royal Victoria Hospital and McGill University, Montreal, Quebec, Canada

We present a correction technique that uses the effective bone and tissue attenuation coefficients to compensate ^{99m}Tc-HMPAO brain SPECT projections for attenuation. Transverse images of a human skull filled with a uniform mixture of ^{99m}Tc and gelatin have a greater count density at the center with respect to the periphery when corrected for attenuation with the effective water/tissue coefficient of 0.12 cm^{-1}. An attenuation coefficient of 0.09 cm^{-1} produces uniform images at the expense of a reduced count density. Additional experiments with phantoms wrapped with aluminum (to simulate bone) indicate that the greater count density at the image center is a result of increased attenuation at the edges of the projections where there is a greater path length through the aluminum (or bone). SPECT projections explicitly corrected for both bone and soft-tissue attenuation result in images of improved uniformity and increased count density.

J Nucl Med 1992; 33:1875–1880

Single-photon emission computed tomography (SPECT) has the potential to be quantitative, where the counts/pixel of a reconstructed image represents the Bq/g of the administered radiopharmaceutical in the patient. However, attenuation is the major limitation of quantitation in SPECT. Attenuation is defined as the reduction of the number of detected gamma rays by photoelectric absorption and Compton scatter. Attenuation also affects the quality of images by reducing lesion contrast and producing "hot rim" artifacts (*1*). Therefore, attenuation must be compensated for to ensure accurate quantitation and to improve the quality of images.

There exist many attenuation corrections which assume that the body is homogeneous and are therefore able to use a constant attenuation coefficient (*2–11*). This assumption is valid for SPECT imaging of the abdomen but it will not provide accurate quantitative information in SPECT imaging of the chest or brain. Iterative attenuation compensation algorithms (*3,6,8,10–13*) correct for variable attenuation and produce more accurate representations of the source distribution. However, these algorithms are computationally intensive.

Brain imaging is unique in that the radioactivity is contained in a homogeneous medium (brain tissue) which is completely surrounded by a medium of different composition (bone). The gamma rays emitted from the radionuclides will be attenuated by the brain tissue and the bone of the skull. When compensating brain images with constant attenuator corrections it is often recommended that the effective tissue coefficient be used (*4,14*), and it has even been suggested, but not proven, that an increased coefficient should be used in order to correct for the additional bone attenuation (*15*). Evidence has been presented to recommend that the effective attenuation coefficient should be reduced and not increased (*16*). Our experimental findings confirm that recommendation, and we propose an attenuation compensation technique for HMPAO brain SPECT images that explicitly corrects the SPECT projections for both bone and soft-tissue attenuation, thereby improving uniformity and increasing the count density.

MATERIALS AND METHODS

Derivation of Attenuation Correction

The attenuation relationship for a projection of a point source in a homogeneous medium is $N = N_o e^{-\mu x}$, where N is the number of counts in the projection for the point source at depth x in the attenuating medium, N_o is the true number of counts of the point source and μ is the linear attenuation coefficient for the appropriate medium and gamma ray energy.

A prereconstruction algorithm which corrects for the bone and tissue attenuation in the projections has been derived from first principles. Its derivation is based on the Sorenson technique (*2*), which has been modified to include an outer medium (bone) which completely surrounds the inner attenuating medium (soft tissue). A complete description of the derivation is included in the Appendix. Prior to reconstruction, the projections are summed then multiplied by the factor:

$$\frac{\mu_t L}{1 - \exp[-\mu_t L]} \exp[\mu_b d_{(x',\theta)}], \qquad \text{Eq. 1}$$

to correct for tissue and bone attenuation, where μ_t and μ_b are

Received Jan. 2, 1992; revision accepted May 28, 1992.

For reprints contact: Brad Kemp, MSc, Nuclear Medicine Department, St. Joseph's Health Centre, 268 Grosvenor St., London, Ontario, Canada N6A 4V2.

the soft-tissue and bone linear attenuation coefficients, respectively, L is the chord length through the tissue and $d(x', \theta)$ is the bone thickness for element x' of the projection angle θ. It is assumed that the skull thickness $d(x', \theta)$ is constant within the slice. The first factor is the water attenuation correction factor, which has previously been derived (*2*). It assumes that the source is uniformly distributed throughout the tissue and is a good approximation for studies such as ^{99m}Tc-hexamethylpropyleneaminoxime (HMPAO). The $\exp[\mu_b d_{(x',\theta)}]$ factor corrects for the bone attenuation and is intuitively correct since it is the reciprocal of the attenuation through the bone, $N/N_o = \exp[-\mu_b d_i]$, where d_i is the path length through the bone at the position i.

Since scatter is not corrected for explicitly, the effective attenuation coefficients for μ_t and μ_b should be used. The effective attenuation coefficients are reduced from the narrow beam value in order to allow for the detected scatter present in the projections (*17*). The effective attenuation coefficient for tissue or water at 140 keV (with a 20% energy window), the gamma ray energy for ^{99m}Tc, is $\mu_w = 0.12\ cm^{-1}$ (*17*). The effective attenuation coefficient for bone will be found from experiment.

A program that uses the derived correction factor (Equation 1) to compensate projections for the bone and brain tissue attenuation has been written in Pascal in the General Electric (Milwaukee, WI) STAR programming environment. The high count density in ^{99m}Tc-HMPAO projections of the brain permits the delineation of the boundary between the bone and brain tissue using the photopeak projections, and it allows for separate contours for each transverse slice (*18*). Each contour is represented by an ellipse found from a least squares fit of the boundary points of the projections which are found using a count threshold technique (*18*).

Human Skull Experiment

A human skull with an average radial thickness of bone of 0.72 cm was filled with a uniform mixture of gelatin (density 1.01 g/cm^3) and 37 MBq of ^{99m}Tc, which represents a clinical ^{99m}Tc-HMPAO study with 740 MBq injection and a 5% uptake in the brain tissue. A SPECT system (General Electric, Starcam 400AC, Milwaukee, WI) was used to acquire a 64 projection data set with a 1.6 zoom, equally spaced over 360° into 64 × 64 matrices (1 pixel is 0.40 cm on edge). The acquisition time was 20 sec per projection and the center of the skull was 16.5 cm from the detector, fit with a low-energy, high-resolution (LEHR) collimator. An energy window of 20% centered on the ^{99m}Tc photopeak was used. All projections were corrected using linearity, energy and uniformity correction files. The projection data sets were reconstructed by filtered backprojection with a ramp filter and a Hanning window with a cutoff at the Nyquist frequency. The transverse images were 1-pixel thick.

To evaluate the effectiveness of the attenuation compensation, a correction ratio was measured. It is defined as the ratio of the mean counts in a central region of interest (ROI) to the mean counts in a peripheral ROI on a reconstructed image (or simply "image"), with a value of one indicating the optimum attenuation correction. An average correction ratio and standard deviation for the human skull image was calculated over 7 slices using central and peripheral ROIs with average areas of 65 and 210 pixels, respectively. The size of the central ROI was drawn as large as possible to improve counting statistics without significantly reducing its value through the inclusion of peripheral pixels. The peripheral ROI was drawn 2 pixels from the image edge. In addition to estimating the effectiveness of the attenuation correction using the correction ratio, profiles 5 pixels wide were taken through the center of a representative image.

Phantom Experiments

To simulate the head, a phantom with an inner diameter of 21.6 cm and 0.3 cm walls was filled with water (to mimic brain tissue) and wrapped with aluminum to simulate the bone of the skull. The aluminum thickness required (x_a) was determined from the following equation:

$$x_a = x_b \rho_b N_{e(b)} / (\rho_a N_{e(a)}), \qquad \text{Eq. 2}$$

where x_b is the thickness of the bone, ρ_b and ρ_a are the densities of bone and aluminum, respectively, and $N_{e(b)}$ and $N_{e(a)}$ are the electron densities of bone and aluminum respectively (*19*). By using $\rho_a = 2.7$ g/cm^3, $\rho_b = 1.66$ g/cm^3, $N_{e(a)} = 2.90 \times 10^{23}$ elect./g and $N_{e(b)} = 3.19 \times 10^{23}$ elect./g (*20*), it is predicted that 0.48 cm of aluminum will replace the 0.72 cm of bone. The actual aluminum thickness used experimentally was 0.51 cm; the discrepancy due to air spaces between layers of the aluminum foil. The aluminum-wrapped phantom was filled with a uniform mixture of 370 MBq ^{99m}Tc in water and positioned with its central axis coincident to the axis of rotation of the detector. A projection data set was acquired and reconstructed with the same parameters used for the human skull study. The Sorenson prereconstruction attenuation correction was used with linear attenuation coefficients of 0.15, 0.12, 0.09, 0.05 and 0.00 cm^{-1} (no correction).

As a reference, the experiments were repeated without aluminum around the phantom to ensure that any error in the attenuation correction was due to the additional aluminum. The reference data set was corrected for the decay between acquisitions and for attenuation with a coefficient of $\mu_w = 0.12\ cm^{-1}$.

An average correction ratio (and standard deviation) was calculated over 8 slices with central and peripheral ROIs of 60 and 210 pixels, respectively. The same central and peripheral ROI was used for all slices. Profiles 7 pixels thick were taken through the image center. The same transverse slices of the phantom with and without aluminum, corrected for attenuation with $\mu_w = 0.12\ cm^{-1}$, and the aluminum-wrapped phantom with $\mu_w = 0.09\ cm^{-1}$ were used to determine the correction ratio and profiles.

Dependence of Aluminum Attenuation on Source Position

To examine the effect of aluminum attenuation with source position, 12.5 cm capillary tubes with an inner diameter of 1 mm were filled with ^{99m}Tc and placed at different locations within the phantom, running axially. Single projections were acquired in a 128 × 128 matrix using a camera with the LEHR collimator 16.5 cm from the phantom center. The energy window was 20% and symmetric about 140 keV. The source was moved parallel to the detector (at a fixed distance from the collimator surface) and located at 0, 8.6, 10.0 and 10.8 cm from the phantom center. The acquisitions of the line source in each location were corrected for decay. Single projections of the phantoms with and without aluminum were acquired for each source position. The activity of the source was low (<15 kcts/sec), eliminating the need for deadtime correction.

A 20-pixel thick profile through each projection was obtained (avoiding the line source ends), and the total counts in the profiles from the static images of the phantom with aluminum (N_w) and without (N_{wo}) for the same source position were determined. The

attenuation ratio N_w/N_{wo} was calculated, which represents the fraction of gamma rays exiting the aluminum for a source at that position.

The effective attenuation coefficient for aluminum was found empirically, calculated from the attenuation ratio $N_w/N_{wo} = \exp[-\mu_{a(eff)}x_a]$, where x_a is the aluminum thickness. The attenuation ratio for a source at the center of the aluminum-wrapped phantom is used because the center is the average depth within the attenuating medium for a 360° SPECT acquisition.

The projections of the aluminum-wrapped phantom filled with uniform ^{99m}Tc in water were corrected using Equation 1 with the effective attenuation coefficients for aluminum and water and the appropriate thickness of aluminum. The corrected projections were reconstructed with the same parameters as before and the correction ratios and profiles of the images determined.

The projections of the human skull were also compensated for attenuation with $\mu_w = 0.09$ cm^{-1} and by using the correction with an effective bone attenuation coefficient set equal to $\mu_{b(eff)} = \mu_{a(eff)}x_a/x_b$ and $\mu_w = 0.12$ cm^{-1}. The correction ratio and profiles were determined from the images.

RESULTS

The correction ratio for images of the human skull corrected with an attenuation coefficient of 0.12 cm^{-1} is 1.05, which indicates that the images are not uniform but have an increased count density at the image center (Fig. 1). For experiments with the aluminum-wrapped phantom, the correction ratio was 1.08, compared to 1.03 for the phantom without aluminum when 0.12 cm^{-1} was used as the effective attenuation coefficient (see Table 1). It is assumed that the correction ratio and profiles for the images without aluminum are correct since the Sorenson correction (*2*) is exact for a uniformly distributed source in a homogenous medium. Therefore, for the phantoms with aluminum, a correction ratio equal to that for the phantom without aluminum will indicate that the effect of the aluminum attenuation has been properly compensated.

TABLE 1
Phantom Corrected for Attenuation

Aluminum	Attention coefficients μ_w (cm^{-1})	Attention coefficients μ_a (cm^{-1})	Correction ratio	Count density
N	0.12	—	1.03*	2000†
Y	0.15	—	1.09	2350
Y	0.12	—	1.08	1900
Y	0.09	—	1.03	1500
Y	0.05	—	0.96	1000
Y	0.12	0.21	1.03	2000

* ±0.01 (1 s.d. for all correction ratios).
† Value at center.

Figure 2 shows that the count density of the profile for the aluminum-wrapped phantom is reduced and nonuniform, as compared to the corresponding profile for the phantom without aluminum. These results imply that an aluminum-wrapped water-filled phantom can be used to simulate the head, and that images of the head (or phantom) have an increased count density at the center. Similar results (not shown) have been obtained from experiments with a 16-cm diameter phantom.

The correction ratios increase if the water attenuation coefficient is increased (Table 1). The best attenuation correction, as defined by the correction ratio, occurs for a coefficient of 0.09 cm^{-1}, but this occurs with a reduction in the count density of the images (Figs. 1 and 2). The count density in an image of the phantom corrected for attenuation with $\mu_w = 0.09$ cm^{-1} is 75% of the count value for the same image corrected with $\mu_w = 0.12$ cm^{-1}.

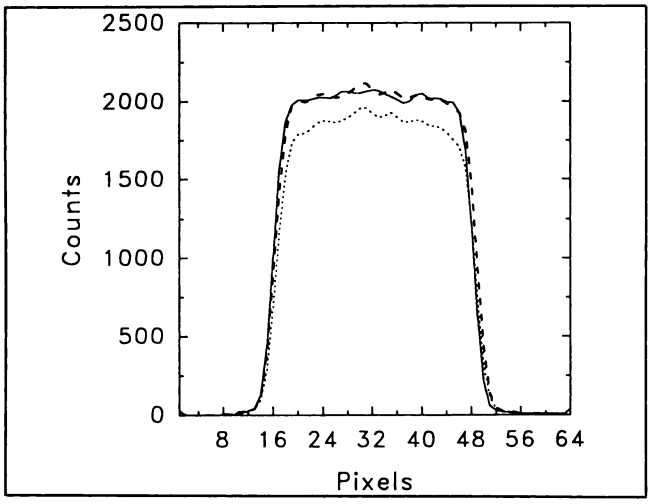

FIGURE 1. Profiles through images of the human skull filled with a uniform mixture of ^{99m}Tc and gelatin. Solid line: image corrected for attenuation with $\mu_w = 0.12$ cm^{-1}; dotted line: image corrected for attenuation with $\mu_w = 0.09$ cm^{-1}; dashed line: image corrected for attenuation with $\mu_w = 0.12$ cm^{-1} and $\mu_b = 0.15$ cm^{-1}. Note the increase in the count density at the center compared to the edges when the image is corrected for water attenuation with $\mu_w = 0.12$ cm^{-1}.

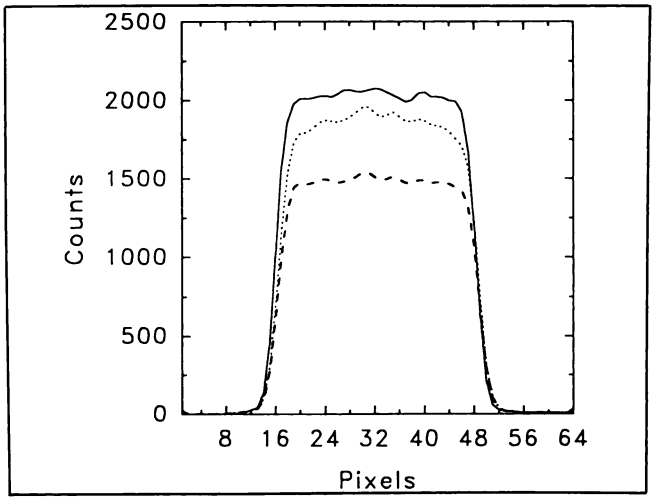

FIGURE 2. Profiles through images of the Jaszczak phantom filled with a uniform mixture of ^{99m}Tc and water. Solid line: phantom without aluminum, $\mu_w = 0.12$ cm^{-1}; dotted line: phantom with aluminum, $\mu_w = 0.12$ cm^{-1}; dashed line: phantom with aluminum, $\mu_w = 0.09$ cm^{-1}.

The effectiveness of the attenuation correction should not be evaluated entirely by the correction ratio, since the count density is also important. However, the correction ratio provides a measure of the uniformity of an image, and for these experiments it indicates that HMPAO brain images corrected for soft-tissue attenuation only are not uniform.

It is evident from Table 2 that the attenuation ratios decrease as the source is moved away from the phantom center, with the ratio being the smallest at the side edge of the phantom. This is due to an increase in the path length through the aluminum as the source is shifted from the center. As a result, the gamma rays must traverse the aluminum obliquely, thereby increasing the attenuation for sources at the side edge of the phantom.

The effective attenuation coefficient for aluminum was found empirically by solving for $\mu_{a(eff)}$ in the attenuation relationship. For a source at the phantom center and an aluminum thickness of 0.51 cm, the effective attenuation coefficient is 0.21 cm^{-1}. This value was used in all the attenuation corrections and is much lower than the narrow beam value of 0.38 cm^{-1} (*20*). The effective bone attenuation coefficient is calculated as 0.15 cm^{-1}.

When the projections of the aluminum-wrapped phantom are compensated for aluminum and water attenuation, the correction ratios are equal to the ratios of the phantom without aluminum (Table 1). In addition, the aluminum attenuation correction creates images with a count density approximately equal to the count density in the images of the phantom without aluminum (Fig. 3). The use of the effective aluminum attenuation coefficient allows for detected scatter due to the aluminum which is present in the projections. The improvement in image uniformity can be seen in the profiles, for they are much flatter and steeper at the edges.

The same general results were found for the images of the human skull, after the projections were corrected for bone and water attenuation (Fig. 1).

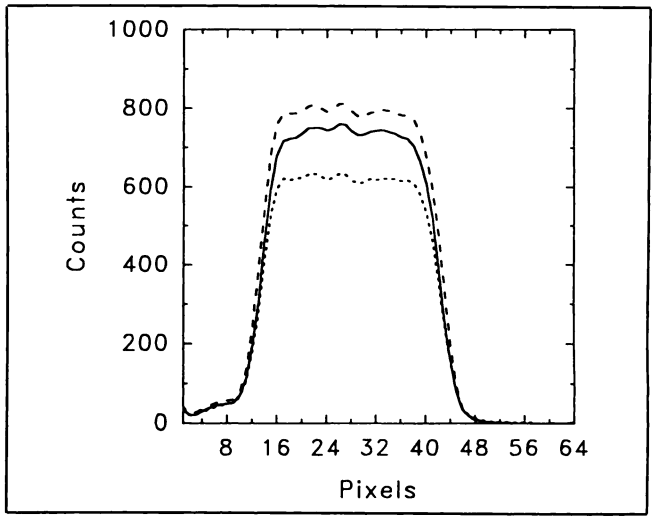

FIGURE 3. Profiles through images of the Jaszczak phantom filled with a uniform mixture of ^{99m}Tc and water. Solid line: phantom without aluminum, $\mu_w = 0.12$ cm^{-1}; dotted line: phantom with aluminum, $\mu_w = 0.12$ cm^{-1}; dashed line: phantom with aluminum, $\mu_w = 0.12$ cm^{-1}; $\mu_a = 0.27$ cm^{-1}.

DISCUSSION AND CONCLUSIONS

Constant attenuator corrections assume that the object is homogeneous and use a fixed attenuation coefficient. SPECT images of the brain are routinely corrected for attenuation with the effective water attenuation coefficient of 0.12 cm^{-1}. This value allows for scatter included in the projections but does not consider the attenuation due to the surrounding skull. The human skull (and phantom) experiments have shown that the skull will decrease the count density of the images, especially at the periphery. This is caused by a greater attenuation at the projection edges where gamma rays must traverse the bone (or aluminum) obliquely. As a result, the count density of images of uniform activity is not constant but is greater at the center. When using the Sorenson technique (*2*), the count density will become uniform only if a reduced [not increased, as previously thought (*15*)] water attenuation coefficient is used. However, the overall count density of the images will be decreased. Clearly, the water attenuation correction alone cannot compensate for both the water and bone attenuation. Our proposed attenuation correction explicitly considers the aluminum (or bone) attenuation in the form of an effective aluminum attenuation coefficient to allow for detected scatter from the aluminum. Consequently, the clinical implementation of the correction will produce SPECT brain images that have increased uniformity and count density, provided the thickness of the skull is known.

Our finding that the skull attenuation reduces the counts detected at projection edges more than at the center will generally affect other attenuation correction techniques besides the one we have explicitly investigated. For example, if the Chang technique (*3*) is derived with an outer layer of nonradioactive bone, the correction factor for each pixel will have an additional $\exp[-\mu_b d_\theta]$ term in the denominator, where d_θ is the bone thickness for that pixel and angle θ. Consequently, our finding is of general interest and should be taken into account whenever an attenuation correction technique is used and the distribution of attenuation coefficients is not directly measured.

TABLE 2
Attenuation Ratios of a Line Source in a Water-Filled Phantom

Distance from center (cm)	Attenuation ratio (N_W/N_{WO})
10.8	0.75*
10.0	0.79
8.6	0.85
0	0.90

* ±0.01 (1 s.d. for all attenuation ratios).

The effective bone attenuation coefficient was calculated from the measured coefficient for aluminum and the calculated value of 0.15 cm^{-1} seems too low. Attempts to measure μ_b explicitly or by using bone equivalent materials (*21*) will be undertaken to determine the validity of our calculations and the possible variability in μ_b between patients.

Clinical implementation of our finding requires that the skull thickness and effective attenuation coefficient be known. Although improvements can be achieved by estimating these values, individual variation in both parameters means that such an approach is questionable. Instead, it would be better to measure these quantities for each patient. One possible approach is to develop a high resolution radionuclide transmission CT technique using ^{99m}Tc as the source. Recent work by Manglos (*22*) indicate that such goals may be achievable using a point source at the focal point of a cone-beam collimator. However, the use of a cone-beam collimator for brain SPECT introduces several problems, particularly image truncation and incomplete sampling (*23*). An alternative approach is to use a line source along the focal length of a fan beam collimator (*18,24*). It is anticipated that such an approach will produce attenuation maps with sufficient resolution which could then be used for attenuation correction of brain SPECT images.

APPENDIX

Derivation of Equation 1

Given that L is the chord length through the brain tissue, let fL be the source length (f is the fractional length of the source along the line $x' = x\cos\theta + y\sin\theta$, where the prime denotes a rotated coordinate system). Let the mean depth of the source in the brain tissue, with attenuation coefficient μ_t, be m, and the constant count rate per unit length C. Also present is the outer layer of bone which completely surrounds the brain tissue and the source distribution. Therefore, the attenuated activity detected at location x′ for the projection angle θ can be represented as:

$$p_a(x', \theta) = \int_{m-fL/2}^{m+fL/2} C\cdot\exp[-\mu_t l]\cdot\exp[-\mu_b d_{(x',\theta)}]dl,$$

where μ_b is the linear attenuation coefficient for bone and $d_{(x',\theta)}$ is the path length through the bone for x′ and projection angle θ. By integrating

$$p_a(x', \theta) = \frac{2C}{\mu_t}\cdot\exp(-\mu_t m)\cdot\exp(-\mu_b d_{(x',\theta)})\cdot\sinh(\mu_t fL/2),$$

the opposing attenuated projection will be:

$$p_a(-x', \theta+\pi) = \int_{m-fL/2}^{m+fL/2} C\cdot\exp[-\mu_t(L-l)]\cdot\exp[-\mu_b d_{(-x',\theta+\pi)}]dl$$

or

$$p_a(-x', \theta+\pi) = \frac{2C}{\mu_t}\cdot\exp[-\mu_t(L-m)]\cdot\exp(-\mu_b d_{(-x',\theta+\pi)})\cdot\sinh(\mu_t fL/2).$$

If the opposing projections are summed:

$$p_a(x', \theta) + p_a(-x', \theta+\pi) = \frac{2C}{\mu_t}\cdot\sinh(\mu_t fL/2)\cdot[\exp[-\mu_t(L-m) - \mu_b d_{(-x',\theta+\pi)}] + \exp[-\mu_t m - \mu_b d_{(x',\theta)}]].$$

To simplify, assume that the source is uniformly distributed within the medium (i.e., f = 1 and m = L/2) and the skull thickness is equal for conjugate views ($d_{(-x',\theta+\pi)} = d_{(x',\theta)}$). Therefore,

$$p_a(x', \theta) + p_a(-x', \theta+\pi) = \frac{4C}{\mu_t}\cdot\sinh[\mu_t L/2]\cdot\exp[-\mu_t L/2]\cdot\exp[-\mu_b d_{(x',\theta)}].$$

If there were no attenuation, the projection would be

$$p(x', \theta) = p(-x', \theta+\pi) = CL.$$

Substitute $C = [p(x', \theta) + p(-x', \theta+\pi)]/(2L)$ and solve for $p(x', \theta)$:

$$p(x', \theta) + p(-x', \theta+\pi) = \frac{[p_a(x', \theta) + p_a(-x', \theta+\pi)]}{1 - \exp[-\mu_t L]}\cdot\mu_t L\cdot\exp[\mu_b d_{(x',\theta)}].$$

Therefore, to correct for tissue and bone attenuation, multiply the sum of the projections by the correction factor

$$\frac{\mu_t L}{1 - \exp[-\mu_t L]}\cdot\exp[\mu_b d_{(x',\theta)}].$$

ACKNOWLEDGMENT

Some of this work was completed by Brad Kemp while he was a MSc student in the Medical Physics Unit at McGill University.

REFERENCES

1. Budinger TF, Gullberg GT, Huesman RH. Emission computed tomography. In: Herman GT, ed. *Image reconstruction from projections: implementation and applications.* New York: Springer-Verlag; 1979:147–246.
2. Sorenson JA. Quantitative measurement of radioactivity in vivo by whole body counting. In: Hine GJ, Sorenson JA, eds. *Instrumentation in nuclear medicine.* New York: Academic Press; 1974:311–348.
3. Chang LT. A method for attenuation correction in radionuclide computed tomography. *IEEE Trans Nucl Sci* 1978;25:638–643.
4. Gullberg GT, Budinger TF. The use of filtering to compensate for constant attenuation in single photon emission computed tomography. *IEEE Trans Biomed Eng* 1981;28:142–157.
5. Bellini S, Piacentini M, Cafforio C, Rocca F. Compensation of tissue absorption in emission tomography. *IEEE Trans Acoustics, Speech, Signal Process* 1979;27:213–218.
6. Budinger TF, Gullberg GT, Huesman RH. Emission computed tomography. In: Herman GT, ed. *Image reconstruction from projections: implementation and application.* New York: Springer-Verlag; 1979:147–246.
7. Tanaka E, Toyama H, Murayama H. Convolutional image registration for quantitative single photon emission computed tomography. *Phys Med Biol* 1984;29:1489–1500.
8. Moore SC. Attenuation compensation in computed emission tomography. In: Ell PJ, Hollman BL, eds. *Emission computed tomography.* New York: Oxford University Press; 1982:339–360.
9. Lewis MH, Willerson JT, Lewis SE, Bonte FJ, Parkey RW, Stokely EM. Attenuation compensation in single-photon emission tomography: a comparative evaluation. *J Nucl Med* 1982;23:1121–1127.
10. Faber TL, Lewis MH, Corbett JR, Stokely EM. Attenuation correction for

SPECT: an evaluation of hybrid approaches. *IEEE Trans Med Image* 1984;3:101–107.
11. Murato K, Itoh H, Mogami H, et al. A comparative study of attenuation correction algorithms in single photon emission computed tomography (SPECT). *Eur J Nucl Med* 1987;13:55–62.
12. Malko JA, Van Heertum RL, Gullberg GT, Kowalsky WP. SPECT liver imaging using an iterative attenuation correction algorithm and an external flood source. *J Nucl Med* 1986;27:701–705.
13. Tsui BMW, Gullberg GT, Edgerton ER, et al. Correction of nonuniform attenuation in cardiac SPECT imaging. *J Nucl Med* 1989;30:497–507.
14. Jaszczak RJ, Greer KL, Floyd CE, Harris CC, Coleman RE. Estimating SPECT count densities, scatter fractions, and statistical noise. *IEEE Trans Nucl Sci* 1985;32:762–768.
15. Croft BY. *Single-photon emission computed tomography.* New York: Year Book Medical Publishers; 1986:241.
16. Nicholson RL, Doherty M, Wilkins K, Prato FS. Paradoxical effect of the skull on attenuation correction requirements for brain SPECT. *J Nucl Med* 1988;29:1316.
17. Harris CC, Greer KL, Jaszczak RJ, Floyd CE, Fearnow EC, Coleman RE. Tc-99m attenuation coefficients in water-filled phantoms determined with gamma cameras. *Med Phys* 1984;11:681–685.
18. Gullberg GT, Malko JA, Eisner RL. Boundary determination methods for attenuation correction in single photon emission computed tomography. In: Esser PD, ed. *Emission computed tomography: current trends.* New York: The Society of Nuclear Medicine; 1983:33–53.
19. Evans RD. *The atomic nucleus.* New York: McGraw-Hill; 1955:672–694.
20. Johns HE, Cunningham JR. *The physics of radiology,* 4th edition. Chicago: Thomas Books; 1983.
21. White DR. Tissue substitutes in experimental radiation physics. *Med Phys* 1978;5:467–479.
22. Manglos SH, Bassano DA, Thomas FD. Cone-beam transmission computed tomography for nonuniform attenuation compensation of SPECT images. *J Nucl Med* 1991;32:1813–1820.
23. Smith BD. Cone-beam tomography: recent advances and a tutorial review. *Opt Eng* 1990;29:524–534.
24. Gullberg GT, Zeng GL, Datz FL, Christian PE, Tung CH, Morgan HT. Review of convergent beam tomography in single photon emission computed tomography. *Phys Med Biol* 1992;37:507–534.

(continued from page 5A)

FIRST IMPRESSIONS

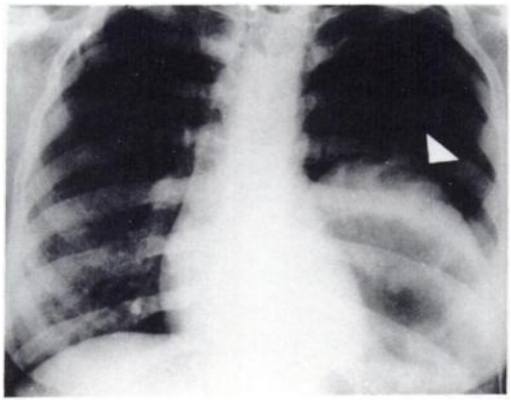

FIGURE 1. An AP chest radiograph demonstrates a large, well-defined space-occupying lesion at the left lower chest (arrow).

PURPOSE
To determine the nature of a lesion adjacent to the left diaphragm. Technetium-99m-sulfur colloid scan depicts intrathoracic ectopic spleen.

TRACER
3 mCi of ^{99m}Tc-sulfur colloid

ROUTE OF ADMINISTRATION
Intravenous

TIME AFTER INJECTION
30 min

INSTRUMENTATION
Scintronix 480–30 Camera

CONTRIBUTOR
Admin Wiqar

INSTITUTION
Nuclear Medicine Centre, Armed Forces Institute of Pathology, Rawalpindi, Pakistan

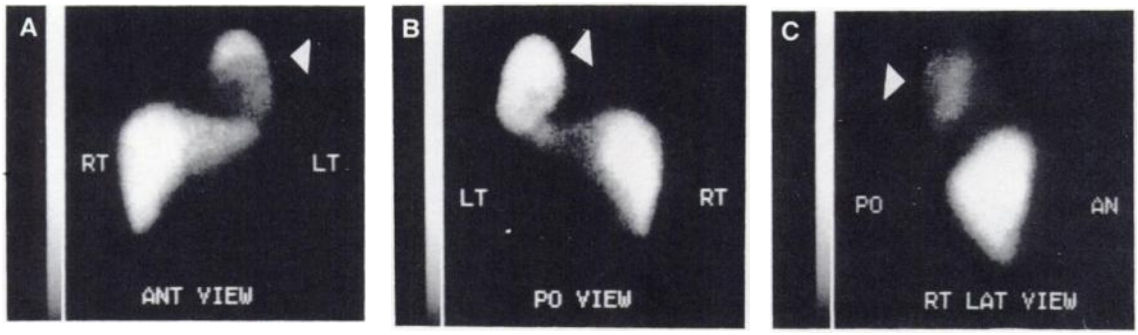

FIGURE 2. (A, B, C) Scintigrams obtained 30 min after i.v. administration of 3 mCi of ^{99m}Tc-sulfur colloid depict the spleen at the left lower chest (arrow). (A) Anterior view, (B) posterior view and (C) right lateral view.